Photothermal trap utilizing solar illumination for ice mitigation

Citation: Dash, Susmita, Jolet de Ruiter, and Kripa K. Varanasi. "Photothermal Trap Utilizing Solar Illumination for Ice Mitigation." Science Advances 4, no. 8 (August 2018): eaat0127. © 2018 The Authors

As Published: http://dx.doi.org/10.1126/sciadv.aat0127

Publisher: American Association for the Advancement of Science (AAAS)

Persistent URL: http://hdl.handle.net/1721.1/120491

Version: Final published version: final published article, as it appeared in a journal, conference proceedings, or other formally published context

APPLIED SCIENCES AND ENGINEERING

Photothermal trap utilizing solar illumination for ice mitigation

Susmita Dash*†, Jolet de Ruiter*‡, Kripa K. Varanasi§

Ice buildup is an operational and safety hazard in wind turbines, power lines, and airplanes. Traditional deicing methods, including mechanical and chemical means, are energy-intensive or environmentally unfriendly. Superhydrophobic anti-icing surfaces, while promising, can become ineffective due to frost formation within textures. We report on a "photothermal trap"—a laminate applied to a base substrate—that can efficiently deice by converting solar illumination to heat at the ice-substrate interface. It relies on the complementing properties of three layers: a selective absorber for solar radiation, a thermal spreader for lateral dispersal of heat, and insulation to minimize transverse heat loss. Upon illumination, thermal confinement at the heat spreader leads to rapid increase of the surface temperature, thereby forming a thin lubricating melt layer that facilitates ice removal. Lateral heat spreading overcomes the unavoidable shadowing of certain areas from direct illumination. We provide a design map that captures the key physics guiding illumination-induced ice removal. We demonstrate the deicing performance of the photothermal trap at very low temperatures, and under frost and snow coverage, via laboratory-scale and outdoor experiments.

INTRODUCTION

Ice buildup via frost formation, condensate freezing, and freezing rain poses significant operational and safety challenges in wind turbines, power lines, residential houses, airplanes, condenser surfaces, and offshore platforms (*1*–*4*). For instance, ice accretion on wind turbines in cold regions and at high altitudes can result in a loss of up to 50% of the annual production (*5*, *6*). Current methods for ice removal include mechanical means, such as raking, shoveling, and hammering, and thermal means, both of which are inefficient and energy-intensive (*7*). Chemical methods include use of deicing fluids and salts that are often corrosive and environmentally unfriendly (*8*).

In recent years, there have been many efforts to delay or prevent ice formation using surface modifications, including superhydrophobic surfaces (*9*–*12*), polymer coatings (*13*), lubricant-impregnated surfaces (*14*, *15*), coatings comprising phase change (*16*), and antifreeze materials (*17*, *18*). The workability of superhydrophobic surfaces is limited under humid conditions because of condensation freezing and frost-induced failure of superhydrophobicity (*19*, *20*), leading to increased ice adhesion. The depletion of the lubricant via cloaking, evaporation, or capillary wicking into the ice structure can deem lubricant-impregnated surfaces unsuitable for long-term anti-icing (*21*). These passive anti-icing methods, though promising, are insufficient to eliminate ice formation. Recent studies have demonstrated the use of plasmonic (*22*–*24*) and magnetic (*25*, *26*) particles to design photothermal surfaces that yield significant temperature increase under absorption of light. However, their scalability is limited by costs and the need for microfabrication, while heating is generally strongly localized to the incident light beam and the immediate vicinity of the particles.

Here, we develop an easily scalable photothermal trap that can use solar or auxiliary illumination for deicing. We study the mechanism governing the photothermally induced melting of ice and develop a phase diagram for the key design parameters. We show that the approach is capable of removing ice, frost, frozen condensate drops, and patches of snow over large surface areas.

Department of Mechanical Engineering, Massachusetts Institute of Technology, Cambridge, MA 02139, USA.
*These authors contributed equally to this work.
†Present address: Indian Institute of Science, Bangalore 560012, India.
‡Present address: Technical University of Denmark, Kongens Lyngby, Denmark.
§Corresponding author. Email: varanasi@mit.edu

RESULTS

Photothermal trap: Mechanism and design

Our photothermal trap consists of three layers: selective absorber, heat spreader, and insulation, as shown in Fig. 1A. The effectiveness of such a trap to deice is defined by the maximum increase in the surface temperature under illumination and the thermal response time scale. These two key factors can be tuned by the design of the photothermal trap. First, it should effectively absorb the incident energy. Second, it should spread the heat laterally while localizing it at the surface. Last, it should have a fast thermal response time so that ice melting and removal are faster than ice buildup, thus preventing ice accumulation. Lateral spreading is critical because often illumination is inhomogeneous due to shadowing of certain surface areas by clouds, objects, or local ice formations, or in cases where solar radiation is insufficient and has to be augmented by a focused external light source. The photothermal trap can be adhered or coated onto an exposed surface to facilitate deicing of the surface (Fig. 1A) and can be realized using commercially available materials.

Here, we use cermet as the selective absorber: It has a high absorptivity α = 95% and a low emissivity of ~3% (see the Supplementary Materials). The low emissivity reduces the heat loss via radiation (*27*). The thin (<1 μm) selective absorber has high in-plane thermal resistance, which necessitates the incorporation of a lateral heat spreader. The heat spreader and the insulation are composed of a 400-μm aluminum layer and commercially available foam, respectively. To highlight the advantage of the complementing properties of the three layers within the photothermal trap, we compare it to three reference cases without a selective absorber (Fig. 1B): an insulating layer with high intrinsic absorptivity (carbon foam) and thick and thin conducting layers (aluminum of thickness 6.3 mm and 400 μm; α = 27% in the visible spectrum). For the single insulating layer, the illumination-induced heat is restricted to the incident area of the beam. For the conductive layers, low absorptivity restricts the extent of temperature rise. Furthermore, for the insulating and thick conducting layers, the long thermal response time can limit the rate of temperature increase. In contrast, our photothermal trap maximizes absorption and minimizes the thermal response time while restricting transverse heat loss, thus yielding maximum temperature rise for a given illumination (Fig. 1B). All reference surfaces have identical foam insulation at the backside to reduce heat loss and are tested under the same illumination conditions as the photothermal trap.

Figure 1A shows the heat transfer processes involved in the system consisting of a frozen water droplet atop the photothermal trap. We are interested in the evolution of surface temperature T because it dictates the melting of ice. The input radiative flux $q''_{in} = \alpha I$ is the absorbed incident radiation that causes a uniform temperature increase of the (metal) heat spreader. The spreader loses heat by conduction into ice and insulation and by convection to the ambient environment. The energy balance for the heat spreader with density ρ, specific heat capacity C_p, and thickness δ is given as

$$\rho C_p \delta \frac{dT}{dt} = q''_{in} - h(1-s)(T - T_{amb}) - s q''_{ice} - q''_{ins} \quad (1)$$

Here, T_{amb} is the ambient temperature, h is the convection heat transfer coefficient to the surrounding air, and s denotes the surface fraction of ice. For the aluminum surfaces, ρ = 2700 kg/m^3, C_p = 900 J kg^{-1} K^{-1}, and δ = 400 μm (standard case). q''_{ice} and q''_{ins} are the heat flux into the ice layer and the insulating layer, respectively. In our laboratory-scale experiments, convection is solely buoyancy-driven, and the magnitude of h depends on the relative difference in substrate and ambient temperature and changes with the transient evolution of the substrate temperature (see the Supplementary Materials for details). Because the selective absorber is less than a micrometer thick, we neglect its thermal mass and resistance in the thermal transport analysis. The transient heat transfer in the ice and insulation layers can be modeled as

$$\rho_{ice} C_{p,ice} (dV_{ice}) \frac{dT_{ice}}{dt} = -\frac{\partial}{\partial x}\left(-k_{ice}\left(A_{b,ice}\frac{\partial T_{ice}}{\partial x}\right)\right)\Delta x - h(dA_{ice})(T_{ice} - T_{amb}) \quad (2)$$

$$\rho_{ins} C_{p,ins} (dV_{ins}) \frac{dT_{ins}}{dt} = -\frac{\partial}{\partial x}\left(-k_{ins}\left(A_{b,ins}\frac{\partial T_{ins}}{\partial x}\right)\right)\Delta x - h_1(dA_{ins})(T_{ins} - T_{amb}) \quad (3)$$

Here, A_b denotes the basal area, dV is the volume, and dA is the surface area (exposed to air) of the discretized control volume; the subscripts denote ice or insulation, and h_1 is the heat transfer coefficient to the surrounding air from the insulating layer (its typical value is 10 W m^{-2} K^{-1}; see the Supplementary Materials for details). For the insulating foam: ρ_{ins} = 100 kg/m^3, $C_{p,ins}$ = 1300 J kg^{-1} K^{-1}, and total insulation thickness L_{ins} = 10 mm. For the ice layer, ρ_{ice} = 916 kg/m^3, $C_{p,ice}$ = 2030 J kg^{-1} K^{-1} (estimated value that depends on ice microtexture and air content), and total ice height L_{ice} = 3.4 mm. The heat flux into the ice and insulation are given by $q''_{ice} = -k_{ice}\partial T_{ice}/\partial x|_{x_{ice}=0}$ and $q''_{ins} = -k_{ins}\partial T_{ins}/\partial x|_{x_{ins}=0}$, where k_{ice} = 1 W m^{-1} K^{-1} and k_{ins} = 0.15 W m^{-1} K^{-1} are the respective thermal conductivities. The coupled governing equations for energy transport through the heat spreader, ice, and insulation are numerically solved to give the transient increase in surface temperature for various laminate design parameters and at different illumination and ambient conditions. The governing equations can be simplified by neglecting the heat loss through the insulation and thermal storage in ice to yield the transient increase of surface temperature as $\Delta T = \Delta T_{eq}(1 - e^{-t/\tau_s})$, where $\Delta T_{eq} = q''_{in}/h_{eff}$ is the increase of surface temperature in steady state, and $\tau_s = \rho C_p \delta / h_{eff}$ is the thermal response time. Here, h_{eff} is the effective heat transfer coefficient given as $h_{eff} = h(1-s) + s\,(hk_{ice}/(hL_{ice} + k_{ice}))$. This simple analytical solution is very illustrative because it predicts the same exponential behavior as the full-scale model and predicts the thermal time scale reasonably well; however, it overpredicts the steady-state temperature rise substantially because it ignores heat loss through insulation and thermal storage in ice. For an accurate estimation of both the steady-state temperature increase of the surface ΔT_{eq} and heating time scale τ_s, we use the full-scale numerical model for comparison with the experimental data.

Freezing and melting behavior

The performance of the photothermal trap is assessed based on laboratory-scale experiments inside a specifically designed cold chamber (Fig. 1C) that allows indirect, homogeneous cooling and then maintains constant ambient temperature (see Materials and Methods). We study the freezing

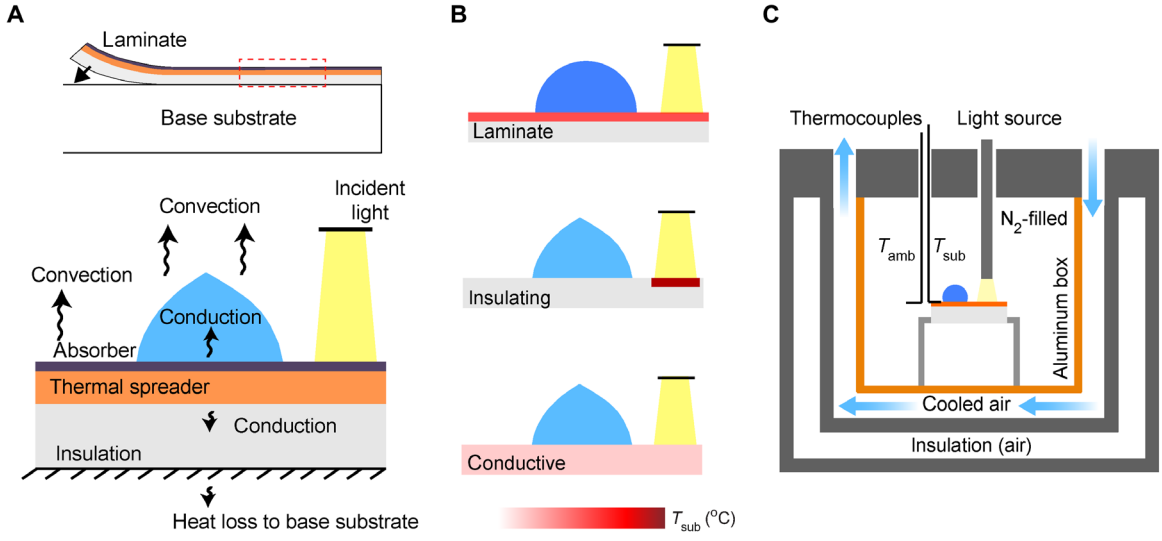

Fig. 1. Concept of photothermal trap for melting of ice. (**A**) Schematic of the photothermal trap applied on the base substrate as a laminate and the associated heat transfer mechanisms. This laminate consists of (top to bottom) highly absorbing cermet, thermal spreader, and insulating layer. The thickness of the absorber layer is exaggerated. (**B**) Heating scenarios for the laminate compared to the reference cases: insulating and conductive layers. The white-to-red color scale indicates the obtained surface heating after a few seconds. (**C**) Sketch of the experimental setup showing separation of the inner experimental chamber (orange) from the environment and the flow of cooling air (blue arrows).

and melting of 40-µl droplets on various test surfaces that have an additional Teflon layer to ensure equal wetting properties (that is, a contact angle of 120°) and clear visualization of the phase fronts. To freeze a droplet, the surface temperature (red curve in Fig. 2A) is slowly decreased by equilibration with a low-temperature ambient environment (black curve). For below-zero surface temperature, the droplet first remains in a supercooled liquid state. We induce the phase transition with a small disturbance (see Materials and Methods). Freezing of the water droplet occurs in two well-known phases (*28*), namely, recalescence and subsequent propagation of the freezing front (*29*). During recalescence, at t = 0 s in Fig. 2A, the supercooled droplet suddenly becomes opaque within ~40 ms (see the left snapshot and movie S1). A fraction of the liquid freezes, forming a slushy mixture of ice crystals and liquid at 0°C (*30*, *31*). Hereafter, the remaining liquid isothermally freezes at a lower rate (in tens of seconds). As the latent heat is released through the high-conductivity surface of the trap, freezing proceeds from bottom to top, as shown in the middle and right snapshots, forming a pointy tip due to the expansion of water upon freezing (*32*, *33*). The temporary increase of the temperature (red curve) during phase change leads to flash evaporation that supersaturates the gas surrounding the droplet, leading to a halo of condensed droplets (shown in the snapshots at 5 and 20 s) (*34*). Slowly, the halo evaporates, and the surface temperature again decreases upon equilibration with the cold ambient environment. The frozen droplet is then equilibrated at the temperature to be studied.

The substrates are illuminated with a halogen light source that has a maximum output radiation of 1.8 kW/m^2 and a spectrum similar to solar radiation. We used maximum power in our laboratory-scale experiments, unless otherwise specified, which amounts to approximately 1.8 times the maximum solar flux, or "1.8 sun." We did additional experiments with 1.0 and 0.5 sun to compare with actual sunlight conditions. Figure 2B shows the thermal response curves upon illumination at an ambient temperature of −25°C. As expected, the insulating foam (gray curve) does not heat up outside the immediate vicinity of the illuminated spot, which we always positioned away from the frozen droplet. For the thick (cyan) and thin (blue) aluminum surfaces, the temperature rise is 15° to 17°C, insufficient to induce melting. However, the thermal time scale reduces by a factor of 10 when reducing the metal thickness from 6.3 mm to 400 µm (from ~600 s to 60 ± 5 s). Our photothermal trap has the same short time scale but, more importantly, combines this with a high-performance selective absorber (cermet) that yields a temperature rise of 50° to 52°C (red curve), thus leading to melting of the frozen droplet. The three snapshots show that melting starts at the droplet-surface interface and propagates upward. The full-scale numerical model (dashed lines in corresponding colors) predicts very well the obtained equilibrium temperatures and time scales, as well as the full temporal temperature increase for nonmelting drops. On the photothermal trap, the latent heat consumed during the phase transition causes a temporary reduction in the rate of increase of the surface temperature, which is not captured by the model (red solid line versus dashed line in Fig. 2B). To avoid this additional energy expenditure, we may illuminate the droplet as soon as recalescence occurs (see Fig. 2C). The melting front then catches up quickly with the arrested freezing front (left snapshot). Subsequently, melting proceeds more rapidly for the mixed ice-liquid droplet than for a fully frozen droplet (two to three times faster). Freezing could be completely eliminated by continuous illumination (keeping the surface temperature high).

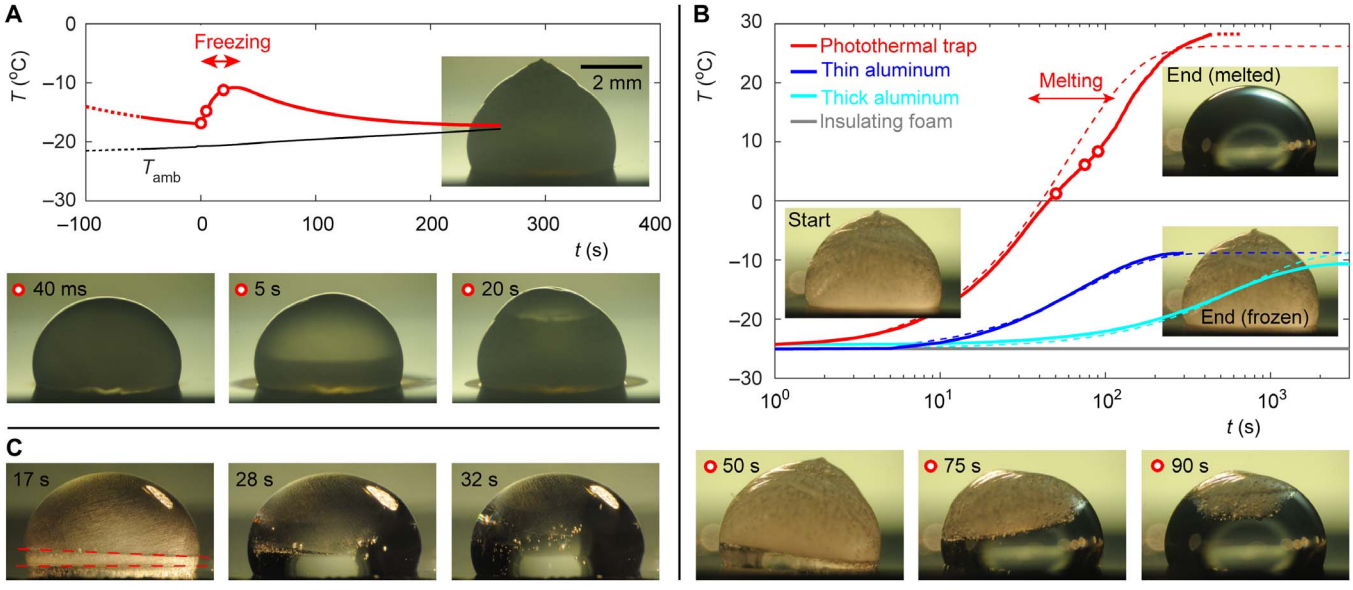

Fig. 2. Single-drop experiments. Freezing (**A**) and melting (**B** and **C**) under an illumination of 1.8 kW/m^2. (A) Change of surface temperature T (red) upon drop freezing at an ambient temperature of approximately −20°C. The ambient temperature increases slightly due to the passive equilibration process (no active cooling). Release of latent heat upon recalescence (t = 0 s) causes an increase in surface temperature and formation of a condensation ring. Snapshots show the progression of freezing (see also movie S1). (B) Change of surface temperature T upon illumination of various surfaces at an ambient temperature of −25°C (h =17.3 W m^{-2} K^{-1}): Only the photothermal trap (red) induces melting, while the droplet placed on a thin aluminum surface (blue), thick aluminum surface (cyan), or insulating carbon foam (gray) remains frozen. The dashed lines show the corresponding model predictions (not accounting for phase change). Insets show the initial frozen droplet (left inset) and final state (melted or frozen; right insets). Snapshots in the lower row show intermediate steps in the progression of melting on the photothermal trap. (C) Representative snapshots of melting on the photothermal trap when illuminated immediately upon recalescence. Left snapshot: The melting front (lower dashed line) catches up with the freezing front (upper dashed line). Here, T_{amb} = −15°C (h =16.7 W m^{-2} K^{-1}). For visualization purposes, and to keep wetting properties constant across all tested surfaces, we coated the surfaces with a ~100-nm Teflon layer, yielding a large contact angle of ~120°; this does not compromise light absorption (see the Supplementary Materials). Initial drop volume is 40 µl, corresponding to a base diameter of 4.6 ± 0.2 mm (s = 0.03) [see scale bar in (A)].

However, because solar illumination is not always continuously and uniformly available, and illumination at the instant of recalescence requires precise monitoring of ice formation, we study the "worst-case" scenario of fully frozen droplets.

Performance diagram: Melting delay and working range

The heat transfer model predicts the ability of the photothermal trap to induce melting. Interfacial melting starts when the surface temperature T increases to zero or, equivalently, when the surface temperature rise due to illumination ΔT overcomes the ambient undercooling (that is, $\Delta T = -T_{amb}$). Setting this value in the exponential curve for ΔT from the full numerical model yields the melting delay t_0, which is the time needed to initiate surface melting after the start of illumination

$$t_0 = -\tau \cdot \ln\left[1 - |\Delta T_{eq}/T_{amb}|^{-1}\right] \text{ provided } |\Delta T_{eq}/T_{amb}| > 1 \quad (4)$$

This melting delay time, under given ambient conditions, thus depends on the thermal properties of the trap that are captured by ΔT_{eq} and τ, predicted by the numerical model. Moreover, surface designs that do not reach a sufficiently high equilibrium temperature, $|\Delta T_{eq}/T_{amb}| < 1$, are unable to induce melting; for example, the aluminum and insulating carbon foam surfaces under the ambient conditions shown in Fig. 2B.

In Fig. 3A, we show the predicted melting time t_0, Eq. 4, as a function of ambient temperature for the photothermal trap and reference surfaces (different colors) illuminated with 1.8 kW/m^2 and with transfer coefficient h = 16.0 to 17.1 W m^{-2} K^{-1} (no shear flow). This forms a "performance" diagram that, for each surface, has two regions: Above t_0, (at least) the surface layer of the droplet is liquid, allowing its instantaneous removal; below t_0, the droplet is completely frozen and stuck. The observed onset of melting in single-drop experiments, as indicated by the colored markers, shows very good correspondence with the numerical prediction.

The superior performance of the photothermal trap can be explained directly from the reduced region of the performance diagram (below t_0) for which the drop stays frozen and has two aspects. First, the photothermal trap has very high ΔT_{eq} ~ 50°C (only slightly varying with ambient temperature), which significantly reduces the area where the drop remains frozen: The asymptote $T_{amb,min}$ is the minimum ambient temperature at which the surface can induce melting [that is, when $\Delta T_{eq}(T_{amb,min}) = T_{amb,min}$]. Obtaining high ΔT_{eq} is of utmost importance to extend the working range of the laminate toward harsh conditions. It can be achieved at high absorptivity α (compared to

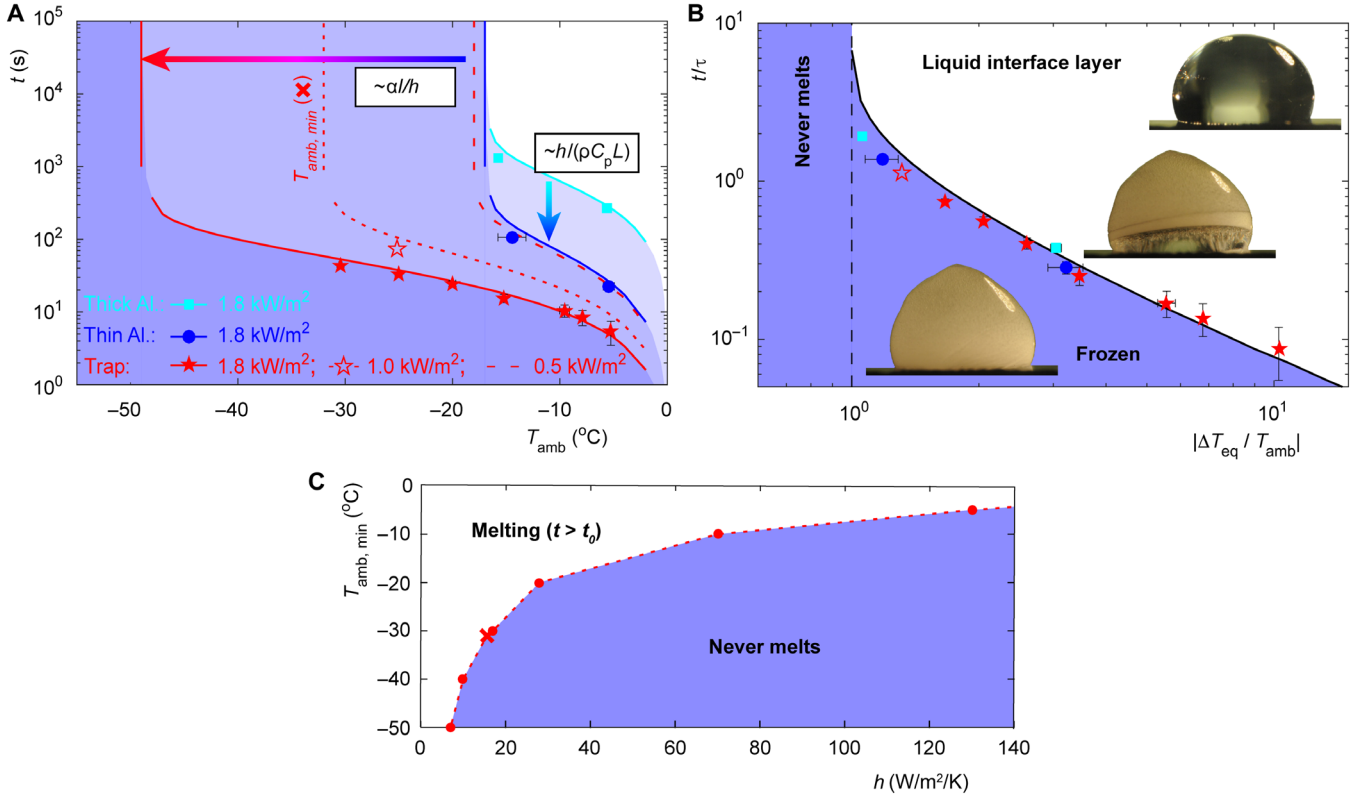

Fig. 3. Performance of photothermal trap versus reference surfaces. (**A**) Performance diagram, showing the melting delay t_0 upon illumination as a function of T_{amb}. Solid colored lines show the numerical results, Eq. 1, for the various substrates (red, blue, and cyan) at an illumination of 1.8 kW/m^2 and an ice coverage fraction s = 0.03. Red dashed lines indicate varying illumination intensity: 1.0 and 0.5 kW/m^2 for the photothermal trap. For each surface, the curves divide the state of the drop into fully frozen (left of the curve) versus, at least partially, melted (right of the curve). The markers show the experimental data. Colored arrows indicate (left) an increase in ΔT_{eq} (shift in asymptote $T_{amb,min}$) with increased absorbed energy and (down) a decrease in time scale τ with decreased thermal mass. (**B**) Nondimensional phase diagram obtained by plotting t_0/τ (black line) as a function of $|\Delta T_{eq}/T_{amb}|$ shows a collapse of data. Left of the asymptote (black dashed line), the droplet remains frozen. Representative snapshots of a 40-μl droplet highlight frozen and melted regions. (**C**) Influence of heat transfer coefficient on photothermal trap performance: minimum ambient temperature $T_{amb,min}$ for which the photothermal trap induces melting, as a function of heat transfer coefficient. Numerical results shown correspond to illumination of the laboratory-scale photothermal trap with 1 kW/m^2 [the cross denotes the asymptote of the red short dashed lines in (A)].

−17°C for uncoated aluminum), at high illumination intensity I (compared to red dashed lines for 1.0 and 0.5 kW/m^2), and at low heat transfer coefficient (discussed in the next section), as indicated by the horizontal colored arrow. Second, for less harsh conditions that do allow melting, eventually, on all tested surfaces, the photothermal trap has the smallest melting delay t_0. Obtaining fast onset of melting, for example, within seconds to minutes, is particularly relevant in cases of fluctuating illumination intensity or to reduce energy consumption when additional illumination [for example, light-emitting diodes (LEDs)] is used. The melting delay is directly proportional to the thermal mass $\rho C_p \delta$, as indicated by the shortened t_0 (vertical colored arrow) comparing a thin aluminum surface (cyan) with a thick aluminum surface (blue). However, with the same thermal mass, the photothermal trap also has superior behavior at any T_{amb} right of the asymptote, because t_0 is also inversely proportional to ΔT_{eq} for conditions of abundant illumination. This can be shown by replotting the performance diagram in Fig. 3B as a function of the nondimensionalized parameters t_0/τ and $|\Delta T_{eq}/T_{amb}|$, which collapses the data on a single curve. This performance diagram accurately predicts the occurrence of melting and its corresponding delay time t_0, based on the surface thermal properties captured by ΔT_{eq} and τ under known ambient conditions.

Application tests

The workability of the photothermal trap strongly depends on the heat transfer coefficient, which can be expressed in terms of the Reynolds number (Re) and the Prandtl number (Pr) in case of forced convection, as (*35*) $h = 0.664 Re^{1/2} Pr^{1/3} (k/L)$, where k is the thermal conductivity and L is the typical length scale. Keeping the thermophysical properties of the air constant, the heat transfer coefficient depends on the length scale and wind velocity (v) as $h \sim (v/L)^{0.5}$. While the large length scales in outdoor applications (typically meters instead of centimeters studied here) lead to lower heat transfer coefficient, strong winds and relative motion can lead to a significant increase of air convection. To demonstrate the limiting effect of the heat transfer coefficient, we use the full-scale numerical model to calculate the workable region of the photothermal trap at an illumination of 1 sun. For varying heat transfer coefficient up to ~100 W m^{-2} K^{-1}, we show in Fig. 3C the minimum ambient temperature $T_{amb,min}$ at which the photothermal trap induces melting: $\Delta T_{eq}(T_{amb,min}) = T_{amb,min}$. A wide workable region exists for buildings, solar panels (*36*), and wind turbines (*6*, *37*) that experience a moderate heat transfer coefficient of a few tens of W m^{-2} K^{-1}. Figure S3 shows a demonstration experiment of melting using an illumination of 1 sun under shear flow conditions (h ~ 70 W m^{-2} K^{-1}). On the other hand, under harsh conditions that are expected for in-flight aircraft conditions (*38*, *39*) with ice-roughened wings (that is, a heat transfer coefficient of hundreds of W m^{-2} K^{-1}), the temperature increase is moderate (a few degrees), and these applications may require additional illumination.

A frozen droplet can be removed from the surface of the photothermal trap by virtue of the melted interfacial layer, thus requiring only a very small fraction of the frozen drop to melt. To demonstrate this, we illuminate a surface with a frozen droplet adhered to it placed at a ~30° angle (see Fig. 4A and movie S3). As soon as the surface temperature reaches 0°C, hereafter 19.8 s, the droplet is dislodged from the surface and starts sliding. Four snapshots show the position of the droplet at 0, 0.5, 0.7, and 1.2 s (all within the small red square on the main panel), with the insets highlighting the presence of the liquid film. The droplet is fully removed within approximately 1 s, as validated by the absence of latent heat effects on the temperature curve. The prompt removal of the ice greatly reduces the energy required for deicing, especially for thicker ice accumulations.

The photothermal trap is effective not only for sparse droplets but also for a variety of ice structures such as a frost layer or a dense layer of frozen condensate droplets. Figure 4B shows illumination of a frost layer fully covering the surface and having a thickness of approximately 1 mm. Melting of the interfacial layer starts at the illumination spot within a few seconds of illumination and propagates along the entire

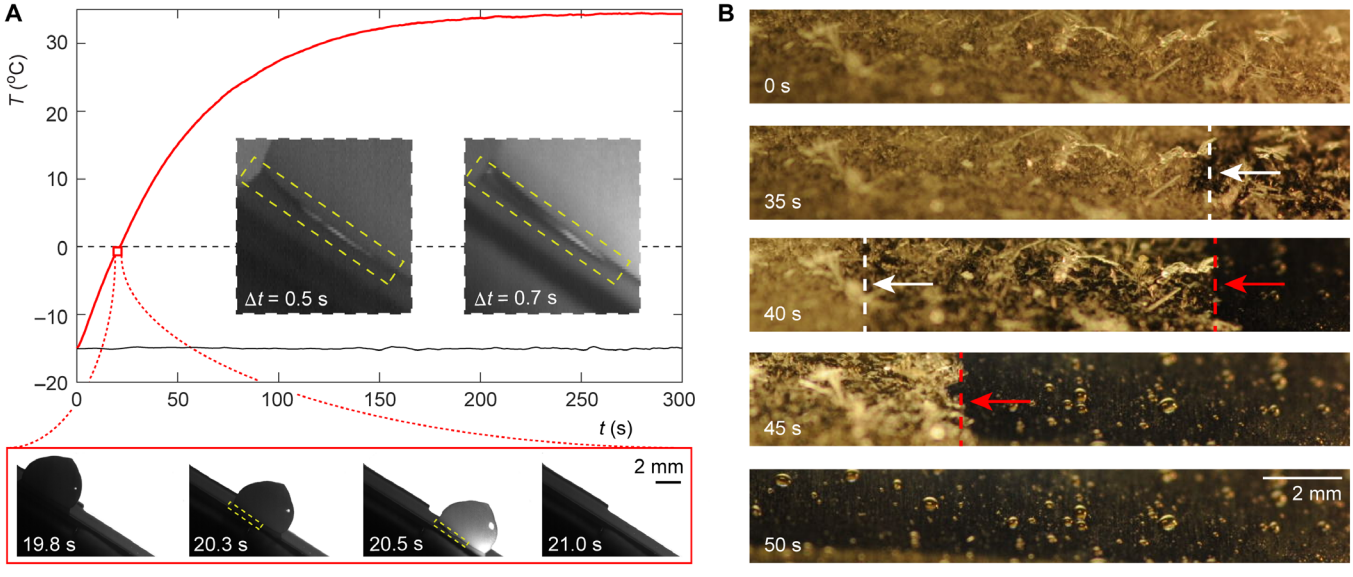

Fig. 4. Application tests. (**A**) Sliding of a frozen drop on a 30° tilted substrate. Sliding starts promptly when a thin liquid film is present (here, 19.8 s after illumination). Insets show the liquid layer 0.5 and 0.7 s after the start of melting (highlighted by yellow dashed boxes). Illumination is at the lower side of the incline, explaining the increase of brightness when the drop starts moving. Drop volume is 40 μl. (**B**) Melting of a frost layer (s = 1). The substrate is illuminated, through the frost layer, at its right side outside the video frame. Melting proceeds from right to left in two stages: First, the surface layer melts (white dashed lines indicate the melting front), followed by bulk melting that allows collection of most of the liquid by dewetting (red dashed lines), leaving only a few residual microdroplets on the surface. Conditions in both panels: an illumination of 1.8 kW/m^2 at an ambient temperature of −15°C.

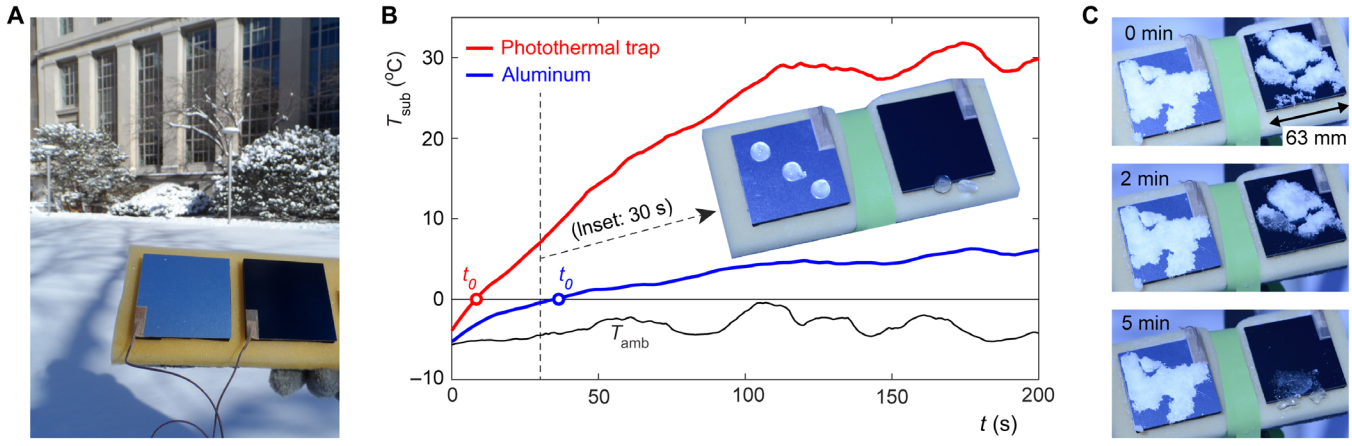

Fig. 5. Outdoor performance. (**A**) The experimental setup is taken outside in Cambridge, MA. It has a thin aluminum surface layer (left) and the photothermal trap (right). Both have areas of 0.004 m^2. Photo credit: J. de Ruiter, Massachusetts Institute of Technology, Cambridge. (**B**) Temperature increase upon illumination, and resulting sliding-off of frozen 0.5-ml puddles (snapshot). The ambient temperature is below zero, and slightly fluctuating, −3.5 ± 1.3°C (black curve), due to variations in wind velocity and sun intensity. The solar intensity is ~0.6 kW/m^2. (**C**) Melting of snow on the photothermal trap, shown at 2 and 5 min after initial exposure to sunlight (t = 0).

length of the test substrate (white dashed lines highlighting the change in contrast; see also movie S4). The propagation of the melt layer is followed by a relatively slower bottom-up melting, leading to the collapse of the frost layer (red dashed lines). Most of the liquid dewets the surface, leaving just a few residual microdroplets as shown in the last panel. Because the surface is initially fully covered with frost, we show that the light is able to penetrate even semi-opaque ice structures.

The final tests are performed outside, on a cold, windy but sunny day (Fig. 5A). We measure a solar intensity of 0.6 ± 0.1 sun during the experiment and an ambient temperature of −3.5 ± 1.3°C. Figure 5B shows the temperature increase of a thin aluminum surface (blue) and the photothermal trap (red) upon exposure to the sun. The surfaces have a similar heating time scale, but the temperature rise on the photothermal trap is more than three times higher: 37°C versus 11°C. The photothermal trap thus shows a quick removal of prefrozen 0.5-ml puddles that slide off the tilted surface as soon as the interfacial layer melts (see the inset in Fig. 5B). For lower ambient temperatures (between −11° and −37°C), the behavior between the photothermal trap and the aluminum surface would show even larger contrast, because the ice would melt on the trap but not on the aluminum surface. For the observed equilibrium temperature increase, the heat transfer coefficient is calculated as $h \sim 10$ W m^{-2} K^{-1}. For increased heat transfer coefficients, the lowest ambient temperature for which the photothermal trap still melts ice at an illumination of 0.6 sun is then estimated to be −21°C at 20 W m^{-2} K^{-1} and −5°C at 100 W m^{-2} K^{-1}, demonstrating the wide applicability of the trap. A partial coverage of snow can also be removed [see Fig. 5C: the interfacial melt layer enables large patches of snow to slide off (lower snapshot)].

DISCUSSION

We have demonstrated the viability of a photothermal trap for deicing. The trap confines heat at the surface and roughly yields an increase in surface temperature of 4°C for an increase in illumination intensity of 0.1 kW/m^2 (which is a tenth of maximum solar intensity) under moderate convection conditions (h = 20 W m^{-2} K^{-1}). We show that solar illumination can result in a temperature rise as high as 33°C, making this an extremely energy-efficient deicing approach. The operability of the photothermal trap can be extended to harsher freezing conditions by using additional illumination such as LEDs. Naturally, operation of LEDs comes with an energy expense that is higher than direct heating methods (due to their maximum 50% energy efficiency). However, our approach allows for one single, flexible design that works under varying illumination conditions—freely available sunlight or augmented light—and does not need additional surface structuring to incorporate alternative heating methods. Our approach can be easily integrated with existing systems and allows for rapid melting of the interfacial ice layer, thus allowing removal using gravity or moderate aerodynamic forces. We expect that this work will open up possibilities to further enhance photothermal deicing by coupling with other effects that induce thermal mismatch or other smart materials such as shape-memory alloys that respond to a change in temperature.

MATERIALS AND METHODS

Laboratory-scale experiments were performed inside a specifically designed cold chamber (Fig. 1C), which allowed for cold, stagnant ambient conditions via conductive cooling. It consisted of a multiwalled box with an inner controlled-atmosphere chamber that is purged with nitrogen before each experiment. It was surrounded by, successively, a shell to circulate cooled air to control the inner chamber temperature, a shell with stagnant air for insulation, and additional foam insulation layers. The cooled airflow was separated from the inner chamber by an aluminum wall that allowed good heat transfer yet blocked any airflow leakage. The inner chamber was thus cooled indirectly and had a stagnant nitrogen atmosphere, unless a shear flow was applied to the inner chamber purposely. The cooling air was brought to the required temperature by flowing it through a slurry of dry ice and acetone at −87.5°C. The sample stage was aligned with a side view port for recording and placed below a halogen fiber light (as model for sunlight) that can be positioned accurately to fully contain the light spot within the test substrate area, but not directly on top of the droplet.

In a typical experiment, a 40-μl liquid droplet was first placed on the test surface. To achieve controlled freezing, the ambient temperature in the experimental chamber was cooled to below −20°C, while the substrate was illuminated to keep its temperature above zero. Subsequently, both illumination and cooling flow were turned off, and the substrate (T) was allowed to equilibrate with the ambient temperature (T_{amb}), as shown

in Fig. 2A. Even close to temperature equilibration, near −20°C, the droplet remained in a supercooled state, so we induced recalescence by a small disturbance in the experimental chamber (an approximately 1-s pulse of cooling flow). Upon recalescence, the droplet temperature rose to 0°C; this temperature is not measured in most experiments because an immersed thermocouple may disturb freezing and melting fronts. The measured surface temperature remained lower (for example, −10°C in Fig. 2A) because most of the released latent heat was consumed to heat up the liquid droplet, and there was limited heat transfer to the surrounding environment (*11*). Upon freezing, the solid droplet assumed a symmetrical pointed shape. The surface and ambient temperature (and thus the frozen droplet) were then carefully equilibrated (typically within 0.5°C) at the value of T_{amb} required for the subsequent illumination experiment. The halogen fiber light supplied a maximum radiation of 1.8 kW/m^2. Upon illumination, a small cooling flow was kept and adjusted to keep the ambient temperature in the inner chamber constant (compensation for small heat losses from the experimental setup). We carefully synchronized recordings of thermocouple temperatures (1 Hz) and videography (24 Hz) to be able to relate freezing and melting events to surface temperature.

SUPPLEMENTARY MATERIALS

Supplementary material for this article is available at http://advances.sciencemag.org/cgi/content/full/4/8/eaat0127/DC1

Section S1. Absorptivity of materials
Section S2. Estimation of temporal temperature rise of the substrate due to illumination
Section S3. Freezing and melting movies
Section S4. Droplet sliding upon illumination
Section S5. Demonstration experiment with forced convection
Section S6. Melting of frost layer
Fig. S1. Sample absorptivity.
Fig. S2. Control volume approach to determine the transient temperature evolution of the metal spreader upon illumination.
Fig. S3. Substrate under direct shear flow.
Movie S1. Droplet freezing.
Movie S2. Droplet melting.
Movie S3. Droplet sliding on melt layer.
Movie S4. Melting of frost layer.

REFERENCES AND NOTES

1. C. C. Ryerson, Ice protection of offshore platforms. *Cold Reg. Sci. Technol.* **65**, 97–110 (2011).
2. N. Dalili, A. Edrisy, R. Carriveau, A review of surface engineering issues critical to wind turbine performance. *Renew. Sustain. Energy Rev.* **13**, 428–438 (2009).
3. A. J. Meuler, J. D. Smith, K. K. Varanasi, J. M. Mabry, G. H. McKinley, R. E. Cohen, Relationships between water wettability and ice adhesion. *ACS Appl. Mater. Interfaces* **2**, 3100–3110 (2010).
4. Y. Boluk, *Adhesion of Freezing Precipitates to Aircraft Surfaces* (Transports Canada, 1996).
5. O. Parent, A. Ilinca, Anti-icing and de-icing techniques for wind turbines: Critical review. *Cold Reg. Sci. Technol.* **65**, 88–96 (2011).
6. P. Suke, *Analysis of Heating Systems to Mitigate Ice Accretion on Wind Turbine Blades* (McMaster University, 2014).
7. M. Farzaneh, C. Volat, A. Leblond, Anti-icing and de-icing techniques for overhead lines, in *Atmospheric Icing of Power Networks* (Springer, 2008), pp. 229–268.
8. D. M. Ramakrishna, T. Viraraghavan, Environmental impact of chemical deicers—A review. *Water Air Soil Pollut.* **166**, 49–63 (2005).
9. J. Lv, Y. Song, L. Jiang, J. Wang, Bio-inspired strategies for anti-icing. *ACS Nano* **8**, 3152–3169 (2014).
10. P. Tourkine, M. Le Merrer, D. Quéré, Delayed freezing on water repellent materials. *Langmuir* **25**, 7214–7216 (2009).
11. T. Maitra, M. K. Tiwari, C. Antonini, P. Schoch, S. Jung, P. Eberle, D. Poulikakos, On the nanoengineering of superhydrophobic and impalement resistant surface textures below the freezing temperature. *Nano Lett.* **14**, 172–182 (2014).
12. J. C. Bird, R. Dhiman, H.-M. Kwon, K. K. Varanasi, Reducing the contact time of a bouncing drop. *Nature* **503**, 385–388 (2013).
13. K. Golovin, S. P. R. Kobaku, D. H. Lee, E. T. DiLoreto, J. M. Mabry, A. Tuteja, Designing durable icephobic surfaces. *Sci. Adv.* **2**, e1501496 (2016).
14. P. Kim, T.-S. Wong, J. Alvarenga, M. J. Kreder, W. E. Adorno-Martinez, J. Aizenberg, Liquid-infused nanostructured surfaces with extreme anti-ice and anti-frost performance. *ACS Nano* **6**, 6569–6577 (2012).
15. S. B. Subramanyam, K. Rykaczewski, K. K. Varanasi, Ice adhesion on lubricant-impregnated textured surfaces. *Langmuir* **29**, 13414–13418 (2013).
16. M. V. Bhamidipati, Methods and compositions for inhibiting surface icing, US7514017B2 (2009).
17. X. Sun, V. G. Damle, S. Liu, K. Rykaczewski, Bioinspired stimuli-responsive and antifreeze-secreting anti-icing coatings. *Adv. Mater. Interfaces* **2**, 1400479 (2015).
18. A. P. Esser-Kahn, V. Trang, M. B. Francis, Incorporation of antifreeze proteins into polymer coatings using site-selective bioconjugation. *J. Am. Chem. Soc.* **132**, 13264–13269 (2010).
19. K. K. Varanasi, T. Deng, J. D. Smith, M. Hsu, N. Bhate, Frost formation and ice adhesion on superhydrophobic surfaces. *Appl. Phys. Lett.* **97**, 234102 (2010).
20. S. Jung, M. Dorrestijn, D. Raps, A. Das, C. M. Megaridis, D. Poulikakos, Are superhydrophobic surfaces best for icephobicity? *Langmuir* **27**, 3059–3066 (2011).
21. K. Rykaczewski, S. Anand, S. B. Subramanyam, K. K. Varanasi, Mechanism of frost formation on lubricant-impregnated surfaces. *Langmuir* **29**, 5230–5238 (2013).
22. H. H. Richardson, Z. N. Hickman, A. O. Govorov, A. C. Thomas, W. Zhang, M. E. Kordesch, Thermooptical properties of gold nanoparticles embedded in ice: Characterization of heat generation and melting. *Nano Lett.* **6**, 783–788 (2006).
23. A. O. Govorov, H. H. Richardson, Generating heat with metal nanoparticles. *Nano Today* **2**, 30–38 (2007).
24. G. Baffou, P. Berto, E. B. Ureña, R. Quidant, S. Monneret, J. Polleux, H. Rigneault, Photoinduced heating of nanoparticle arrays. *ACS Nano* **7**, 6478–6488 (2013).
25. T. Cheng, R. He, Q. Zhang, X. Zhan, F. Chen, Magnetic particle-based super-hydrophobic coatings with excellent anti-icing and thermoresponsive deicing performance. *J. Mater. Chem. A* **3**, 21637–21646 (2015).
26. X. Yin, Y. Zhang, D. Wang, Z. Liu, Y. Liu, X. Pei, B. Yu, F. Zhou, Integration of self-lubrication and near-infrared photothermogenesis for excellent anti-icing/deicing performance. *Adv. Funct. Mater.* **25**, 4237–4245 (2015).
27. G. Ni, G. Li, S. V. Boriskina, H. Li, W. Yang, T. J. Zhang, G. Chen, Steam generation under one sun enabled by a floating structure with thermal concentration. *Nat. Energy* **1**, 16126 (2016).
28. W. D. King, Freezing rates of water droplets. *J. Atmos. Sci.* **32**, 403–408 (1975).
29. G. Graeber, T. M. Schutzius, H. Eghlidi, D. Poulikakos, Spontaneous self-dislodging of freezing water droplets and the role of wettability. *Proc. Natl. Acad. Sci. U.S.A.* **114**, 11040–11045 (2017).
30. J. Blake, D. Thompson, D. Raps, T. Strobl, Simulating the freezing of supercooled water droplets impacting a cooled substrate. *AIAA J.* **53**, 1725–1739 (2015).
31. S. Jung, M. K. Tiwari, N. V. Doan, D. Poulikakos, Mechanism of supercooled droplet freezing on surfaces. *Nat. Commun.* **3**, 615 (2012).
32. O. R. Enríquez, Á. G. Marín, K. G. Winkels, J. H. Snoeijer, Freezing singularities in water drops. *Phys. Fluids* **24**, 91102 (2012).
33. A. G. Marín, O. R. Enríquez, P. Brunet, P. Colinet, J. H. Snoeijer, Universality of tip singularity formation in freezing water drops. *Phys. Rev. Lett.* **113**, 54301 (2014).
34. S. Jung, M. K. Tiwari, D. Poulikakos, Frost halos from supercooled water droplets. *Proc. Natl. Acad. Sci. U.S.A.* **109**, 16073–16078 (2012).
35. F. P. Incropera, D. P. DeWitt, *Fundamentals of Heat and Mass Transfer* (Wiley, 2002).
36. J. A. Palyvos, A survey of wind convection coefficient correlations for building envelope energy systems' modeling. *Appl. Therm. Eng.* **28**, 801–808 (2008).
37. X. Wang, E. Bibeau, G. F. Naterer, Experimental correlation of forced convection heat transfer from a NACA airfoil. *Exp. Therm. Fluid Sci.* **31**, 1073–1082 (2007).
38. H. J. Allen, B. C. Look, *A Method for Calculating Heat Transfer in the Laminar Flow Region of Bodies* (National Advisory Committee for Aeronautics, 1942).
39. G. Fortin, J.-L. Laforte, A. Ilinca, Heat and mass transfer during ice accretion on aircraft wings with an improved roughness model. *Int. J. Therm. Sci.* **45**, 595–606 (2006).

Acknowledgments

Funding: We acknowledge funding from Alstom. J.d.R. acknowledges a Rubicon fellowship from the Netherlands Organisation for Scientific Research. **Author contributions:** S.D., J.d.R., and K.K.V. designed the research. S.D. and J.d.R. performed the research. S.D., J.d.R., and K.K.V. analyzed the data and wrote the manuscript. **Competing interests:** S.D., J.d.R., and K.K.V. are authors on a U.S. provisional patent application related to this work (62/659955, filed 2018). The authors declare no other competing interests. **Data and materials availability:** All data needed to evaluate the conclusions in the paper are present in the paper and/or the Supplementary Materials. Additional data related to this paper may be requested from the authors.

Submitted 16 January 2018
Accepted 27 July 2018
Published 31 August 2018
10.1126/sciadv.aat0127

Citation: S. Dash, J. de Ruiter, K. K. Varanasi, Photothermal trap utilizing solar illumination for ice mitigation. *Sci. Adv.* **4**, eaat0127 (2018).

Photothermal trap utilizing solar illumination for ice mitigation

Susmita Dash, Jolet de Ruiter and Kripa K. Varanasi

Sci Adv **4** (8), eaat0127.
DOI: 10.1126/sciadv.aat0127